Bulletin of the Seismological Society of America, 91, 3, pp. 427–440, June 2001

Inferring Segment Strength Contrasts and Boundaries along Low-Friction Faults Using Surface Offset Data, with an Example from the Cholame-Carrizo Segment Boundary along the San Andreas Fault, Southern California

by George E. Hilley, J Ramón Arrowsmith, and Elizabeth Stone

Abstract Rupture segmentation arises from changes in fault geometry and strength. We use boundary element models of frictionless strike-slip fault segments to quantify how fault geometry and strength change earthquake surface offset distributions. Using these relationships between fault geometry, strength, and surface offsets, we can infer fault strength from the surface offsets in cases where the fault geometry can be independently constrained. This article includes normalized plots of the surface offset distribution expected from rupture along low-friction fault segments with strength contrasts of 1/4, 1/3, 1/2, 1, 2, 3, and 4 for a range of fault segment geometries. These plots may be used with offset data to constrain the strength of two coplanar, adjacent fault segments. This analysis is applied to the Cholame and Carrizo segments of the San Andreas Fault. The available surface offset data suggest that the offset increases where the fault deepens; in addition, the observed offset gradient at the segment boundary requires a 2/3–1/4 strength ratio of the Cholame to the Carrizo segment.

Introduction

Variations in fault strength, geometry, and loading distribution may result in rupture segmentation (e.g., Day, 1982; Ward, 1997). This segmentation is manifest by consistent spatial and temporal rupture behavior that may be used to forecast the timing and magnitude of future events (e.g., Schwartz and Coppersmith, 1984; WGCEP, 1988; WGNCEP, 1996). Large changes in earthquake surface offsets across segment boundaries may result from changes in fault geometry, strength, or prestresses. For adjacent fault segments, those with larger surface area and stress drop have higher peak offsets (e.g., Segall and Pollard, 1980) (Fig. 1). During rupture, a segment may act as an independent seismic source (e.g., 1979 Imperial Valley earthquake) or may rupture with adjacent fault segments (e.g., 1940 Imperial Valley earthquake) (Thomas and Rockwell, 1996).

Where segment depths can be constrained by geological or geophysical data, the surface offset distribution of an earthquake may be interpreted with mechanical models to estimate the fault segment strength contrast. We calculated the surface offset distribution along coplanar adjacent strike-slip fault segments to examine how it was affected by changing segment depths and strengths. These results are intended as a paleoseismological tool to constrain the strength contrast between adjacent fault segments. Using this method, we estimated the segment strength contrast between the Cholame and the Carrizo segments of the San Andreas Fault (SAF), southern California. The reconstruction and analysis of the 1857 Fort Tejón Earthquake offset distribution suggests a 2/3–1/4 strength ratio between the Cholame and Carrizo segments.

Models of Coseismic Surface Offset Along Faults of Different Geometry and Strength

Modeling Fault Segment Friction, Strength, and Geometry

Mechanical models of fault movement allow us to interpret observations of slip during an earthquake in terms of the stresses that caused the slip (e.g., Wald and Heaton, 1992; Ward, 1997). When rectangular faults experience a constant stress drop, the surface offset distribution is elliptical, and the offset magnitude at each point increases with increasing stress drop and fault length (Fig. 1). Also, as the depth to the bottom tip of a vertical strike-slip fault decreases, so does the magnitude of the surface offset at each point. If depth and/or stress drop along the fault strike increases, so too will the surface offset in those areas. Where we can reconstruct the surface offset distribution for one or

more events and can constrain the dimensions of the fault plane, we can estimate the stress drop during each event and how it must change along the strike of the fault.

Fault strength is defined to be the maximum shear traction a fault can sustain before failure. The Coulomb failure criterion relates fault strength to the normal tractions acting along the fault plane and the cohesion of the fault plane (Jaeger and Cook, 1969):

$$|\tau_s| - (\mu(\sigma_n - p) + c) \geq 0 \qquad (1)$$

where τ_s is the shear traction acting along a surface, μ is the coefficient of friction, σ_n is the normal traction acting on a surface (compression positive), c is the cohesion along the surface, and p is the pore pressure.

If the fault friction (μ) is low, then the shear strength of the fault is nearly equal to the fault plane cohesion (c) and should not be affected by lithostatic stresses (Zoback *et al.,* 1987).

We model a fault segment as a planar crack that undergoes a uniform stress drop. The frictionless crack is embedded in a homogeneous, linear, elastic half-space and is in mechanical quasi-static equilibrium (Segall and Pollard, 1980). We neglect inertial forces in our analysis that have been studied by others (e.g., Andrews, 1976; Day, 1982; Andrews, 1994; Ben-Zion and Rice, 1995). Different magnitude stress drops across different portions of the fault surface are applied to simulate strength contrasts. The assumption of low friction allows us to ignore the effects of lithostatic loading on the fault surface, which may vary spatially along the fault. Implicit in our assumptions is the requirement that all segments of the fault are equally close to failure in order to infer strength from stress drop.

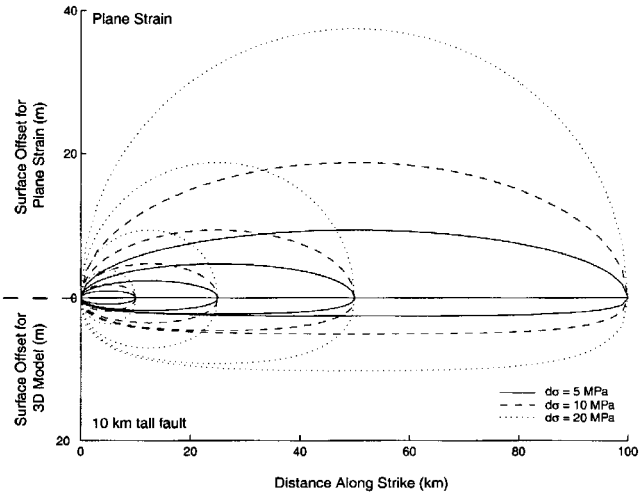

Figure 1. Surface offset produced by a uniform shear stress drop along rectangular faults that are 10, 25, 50, and 100 km long. In these models, a shear modulus of $G = 40$ GPa and a Poisson's Ratio of $\nu = 0.25$ were used. The upper half of the figure shows surface offsets predicted by a 2D plane-strain (infinitely deep fault) model, while the bottom half shows faults that terminate at a 10 km depth. The solid, dashed, and dotted curves show surface offset for stress drops of 5, 10, and 20 MPa, respectively. As strike-slip faults become shorter, peak offset for a given stress drop decreases. Changing stress drop also changes the surface offset distribution.

We use the elastic dislocation model DIS3D (Erikson, 1987; as modified by Rubin, 1988), which uses rectangular dislocations driven by displacement discontinuities acting across element surfaces. Rubin's (1988) modifications allow traction boundary conditions acting across subelements in a rectangular dislocation loop. Slip along a patch results in loading on all other parts of the fault, so each patch is iteratively slipped until the stresses acting across each part of the fault plane satisfies the prescribed boundary conditions (following the methods of Muskhelishvili, 1954; Sokolnikoff, 1956). In our models, we simplify the faulting process by assuming that a total stress drop occurs along each fault segment. In addition, the sum of the coseismic and postseismic displacements release a comparable amount of stress as a coseismic rupture would if the displacements were entirely coseismically produced. Because paleoseismic studies, and particularly, geomorphic offsets record near-fault deformation, offsets should be insensitive to postseismic displacements that result from viscous relaxation of the lower crust following seismic rupture (e.g., Pollitz, 1992; Sieh, 1996; Bürgmann *et al.,* 1997). Also, we neglect dynamic rupture propagation effects and fault prestresses in our analysis. Finally, our models do not capture the behavior of continuously creeping faults such as the Hayward fault and should not be applied to these types of faults.

The case of two planar, vertical, surface-rupturing, strike-slip fault segments, one of which is deeper than the other, was modeled (Fig. 2). The assumption of low fault friction allows the fault segment geometry to be cast as three ratios: (1) the length of the shallow segment normalized to the total fault length (a/c), (2) the difference in depth between the shallow segment and the deeper segment normalized by the depth of the deep segment (e/d), and (3) the ratio

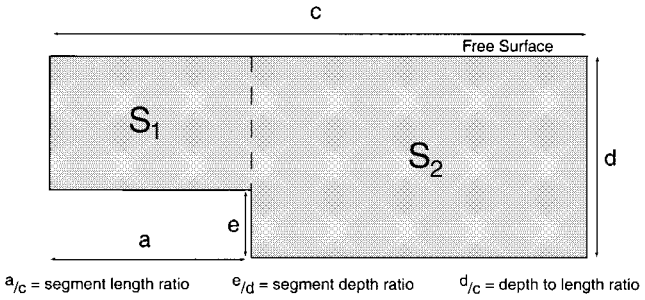

Figure 2. Fault segment geometry of two rectangular, vertical fault segments is defined by three ratios: (1) the segment length ratio (a/c), (2) the segment depth ratio (e/d), and (3) the depth to length ratio (d/c). The strengths of the short and tall segments are S_1 and S_2, respectively.

of the depth of the deep segment to the total fault length (d/c). In our models, we divide the fault plane into 800–896 rectangular elements that each slip an amount required to produce the constant prescribed stress drop along the fault surface.

Results

We varied segment geometries and relative strengths to determine their effect on the surface offset distribution. In all models, the offset at each point was normalized to the maximum offset along the surface rupture. The complete slip distribution along the entire fault plane for all parameter combinations is available at *http://activetectonics.la.asu.edu /segmentation/.*

The Effect of Fault Segment Geometry on Surface Slip Distribution. First, we explored the effect of relative segment length on the surface offset distribution (a/c; Fig. 3). We fixed $e/d = 1/2$ (largest depth contrast) and $d/c = 1/8$ (the least depth/length ratio; Fig. 2), and chose a strength ratio $S_1/S_2 = 1$ (where S_1 and S_2 are the strengths of the short and tall segments, respectively). Areas of high relative offset were concentrated along the deeper segment (Fig. 3a). When the surface offset was normalized to the largest value of all of the curves sampled in Figure 3a, we observed that faults with greater surface area produced larger offsets than those with smaller surface area (Fig. 3b). The magnitude of the offset gradient was insensitive to the fault segment length ratio. However, the location of the maximum value of the offset gradient was strongly influenced by the location of the fault segment boundary (Figs. 3c, d).

We isolated the effect of depth differences between the two segments by fixing $a/c = 1/2$ (equal segment lengths) and $d/c = 1/8$ (minimum value). The strengths of the two segments were equal. The offset distribution was normalized to the maximum value within each model (Fig. 4a) or to all models (Fig. 4b). The surface offset distribution was not significantly shifted along strike as the depth contrast increased. The offset gradient calculated from either Figure 4a or b showed that large depth contrasts resulted in a steeper offset gradients relative to small depth contrasts (Figs. 4c, d).

Finally, we considered the effects of decreasing total fault depth relative to fault length (d/c; Fig. 2). We fixed $a/c = 1/2$ (equal segment lengths), $e/d = 1/2$ (maximum depth contrast), and $S_1 = S_2$. The location of the peak offset moved toward the deeper segment with increasing depth/length ratio (Fig. 5a, b). Increasing d/c moved the corner of the fault segment pair farther from the free surface, which steepened the offset gradient in these models (Fig. 5c, d). Figure 5b also shows that increasing rupture area resulted in larger peak offsets.

The Effect of Relative Segment Strength on Surface Offset Distribution. We considered two segments with fixed geometry and varied the relative segment strength. Figure 6 shows the geometry of two fault segments of equal length ($a/c = 1/2$), the depth of one half that of the other ($e/d = 1/2$). The maximum depth of the deeper segment equaled the length of both of the segments ($d = c$). In order to highlight the effect of segment strength, we varied the strength ratio of the shallower to deeper segment between 1/4 and 4. For higher strength contrasts, the peak offset was skewed toward the segment with higher strength, and hence, higher stress drop during rupture (see Figs. 6a, b). In addition, increasing strength contrast between the two segments resulted in a higher offset gradient at the segment boundary (Fig. 6c, d).

Combined Effects of Fault Segment Geometry and Fault Strength. Figure 7 shows the surface offset distributions from all geometry and strength combinations. The effects of fault geometry and strength were the following: (1) deeper segments had higher peak offset than shallower segments, (2) segments with a greater length-to-depth ratio had higher peak offset than those with smaller length to depth ratios, (3) large depth contrasts between segments resulted in higher offset gradients at the segment boundary, (4) peak offset was skewed towards the segment with the larger surface area, and (5) the peak offset was skewed toward the segment with greater strength. These rules are manifest by the different offset distributions in Figure 7.

Because the information presented in Figure 7 was normalized to the fault geometry ratios, the results may be used for any fault scale for which the friction is assumed to be low, and no significant deviations in the fault strike exist. To use these diagrams, estimate the geometry ratios (a/c, e/d, d/c) using the relevant geological and/or geophysical data (e.g., map trace geometry and microseismicity). Normalize the surface offset distribution by dividing each value of the surface offset by the peak surface offset. Finally, estimate a range of strength contrasts by plotting the normalized offset data on the appropriate graph in Figure 7. In the following sections, we apply this analysis to the Cholame-Carrizo segment boundary of the SAF.

Analysis of Offsets Along the Cholame and Carrizo Segments of the San Andreas Fault

We inferred strength contrasts between the Carrizo and Cholame segments of the SAF using models of fault segmentation. This area was chosen because (1) abundant offset data exist, allowing us to reconstruct the offset distribution of past events with some degree of confidence; (2) the SAF is thought to be a weak fault (e.g., Zoback *et al.,* 1987; Hickman, 1991), justifying the use of our frictionless model; and (3) the Cholame segment may act as an interface between locked (Carrizo) and creeping (Parkfield) portions of the SAF and so plays an important role in forecasting large earthquakes in Southern California (Arrowsmith *et al.,* 1997). Geomorphic offsets were used because they are typically the most abundant offset data. However, geomorphic offsets may record the effects of one or more earthquakes,

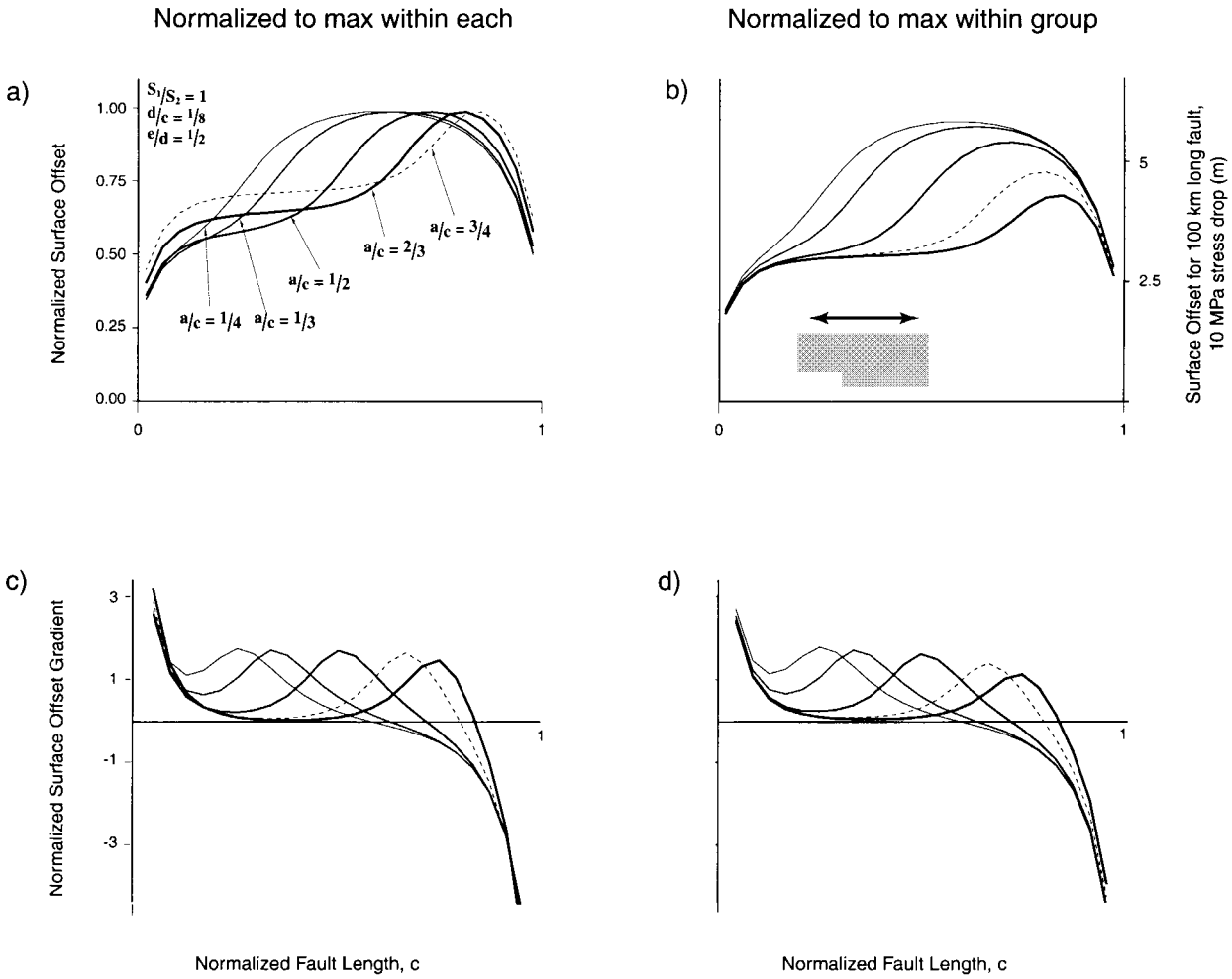

Figure 3. The effect of changing segment length (a/c). (a) The surface offset is normalized to the maximum offset along each fault. The position of the maximum slip is affected by the length ratio of the two segments and is located at approximately the center of the deeper segment. (b) The surface offset normalized to the maximum offset of all models. The magnitude of the maximum offset increases with increasing combined segment surface area. The offsets shown on the right side of the axis correspond to those expected from a 100-km-long fault ($c = 100$ km) that has a 10 MPa stress drop along its surface. For this calculation, $G = 40$ GPa, $\nu = 0.25$. (c) The gradient in the surface offset distribution computed from (a) illustrates that the position of the peak offset gradient is located at approximately the segment boundary. (d) The gradient in the surface offset distribution computed from (b) shows that segments with larger surface area have steeper gradients than segments with less surface area.

differential uplift of the surface during rupture events, and/or geomorphic events that may not be the direct result of tectonic processes (e.g., Lienkaemper and Sturm, 1989).

Several datasets were analyzed (Sieh, 1978; Sieh and Jahns, 1984; Lienkaemper and Sturm, 1989; Lienkaemper, submitted) to reconstruct the surface offset distribution resulting from events along the Cholame and Carrizo segments (Fig. 8). Sieh (1978) provided a fully annotated table that allowed us to compile offsets and their associated uncertainties directly. Sieh and Jahns' (1984) data were extracted from offset diagrams (Sieh and Jahns, 1984; their figure 10), and Lienkaemper and Sturm's (1989) were included directly. In the Sieh and Jahns (1984) dataset, both new data and resurveyed data from Sieh (1978) were presented. We estimated duplicate points by comparing values extracted from Sieh and Jahns (1984) to the Sieh (1978) dataset and removing duplicate or similar values. Also, Lienkaemper (submitted) provided us with offsets, uncertainties, and notes for the Cholame segment.

Because a given offset may record one or more offset events, we filtered the surface offset data to determine the most likely offset distributions. The method used to reconstruct this offset distribution considers the measurement uncertainties, the observer's confidence that offsets were tec-

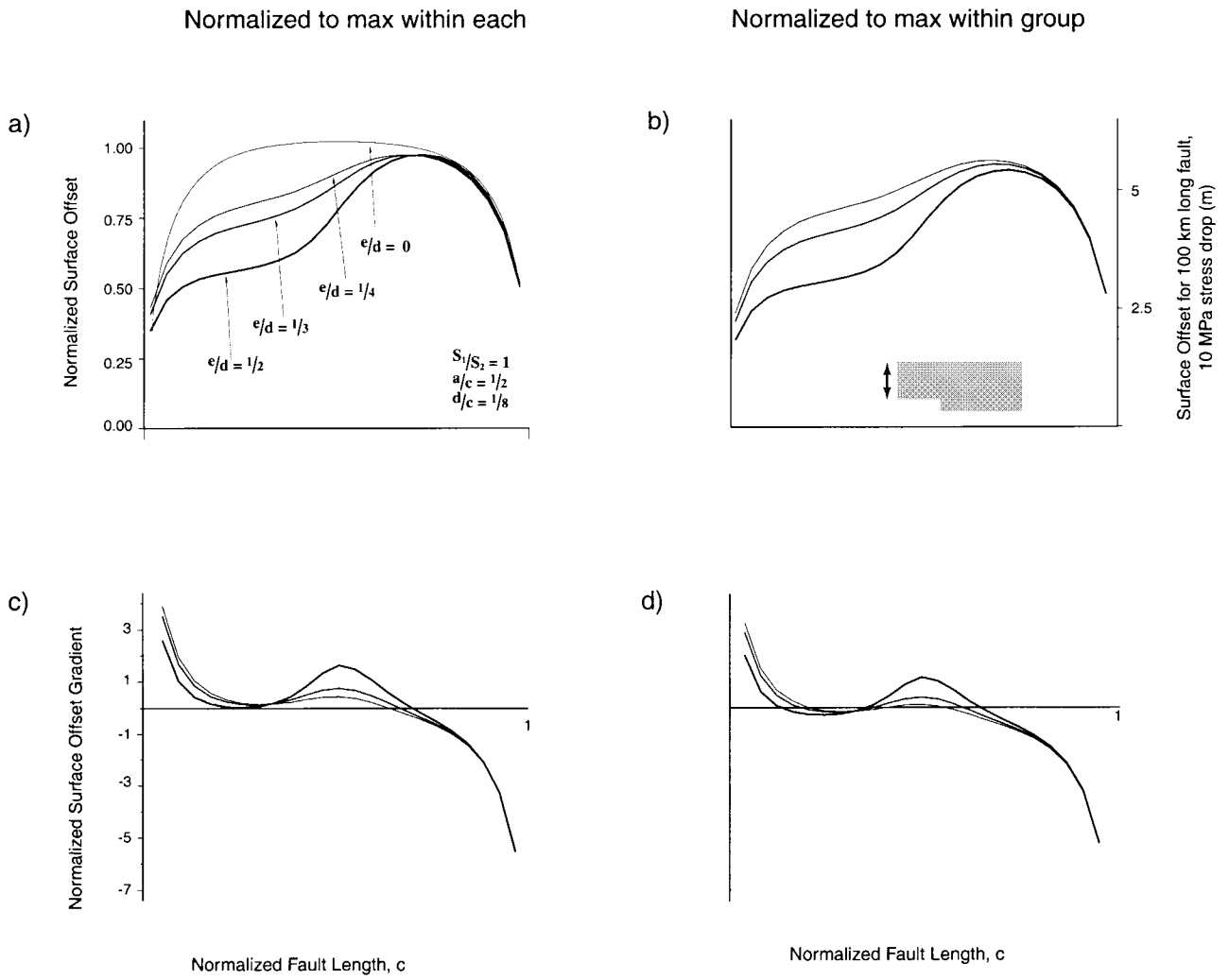

Figure 4. The effect of changing relative segment depth (*e/d*). Segments with greater depth contrasts (increasing *e/d*) have higher slip gradients at the segment boundary. The location of the normalized peak slip is relatively unaffected by the depth ratio. Letters refer to the same normalizations as in Figure 3.

tonically generated, and the observer's bias for each point. First, we treat each offset measurement and associated uncertainty as a normal distribution whose mean and standard deviation are the measurement and half the uncertainty, respectively. Then, we weight the normal distribution according to the observer's confidence that the offset was tectonically generated. Finally, we weight the normal distributions by each observer to estimate the sensitivity of our results to differences in each observer's data collection methods. The normal distributions within a particular interval along the fault were added in order to reconstruct the surface offset within that interval. Where many offsets along the interval are similar, the frequency will be high at the probable value of the offset. In this case, one or more potential tectonic offsets within the interval may be present. We approximate a continuous offset distribution by moving the interval along the fault and identifying potential tectonic offsets. Three sampling intervals were used in this study: 5, 10, and 20 km. Each of these sampling intervals is started at Cholame (0 km) and incremented 1 km along the fault trace. Small, medium, and large dots in Figure 9 denote these most probable potential tectonic offsets for 5-, 10-, and 20-km sampling intervals, respectively. The dots were located at the midpoint of each sampling interval. The left and right graphs show the effect of observer bias on the most likely surface offset distribution, which is subtle. Where few or no data are available, the slip distribution is poorly defined.

Offset Along the Cholame and Carrizo Segments of the San Andreas Fault

We determined the most likely offset distribution for different events along the Cholame and Carrizo segments based on our data filtering and interpretation methods (Fig. 9). Weighting Lienkaemper's data more strongly than Sieh's

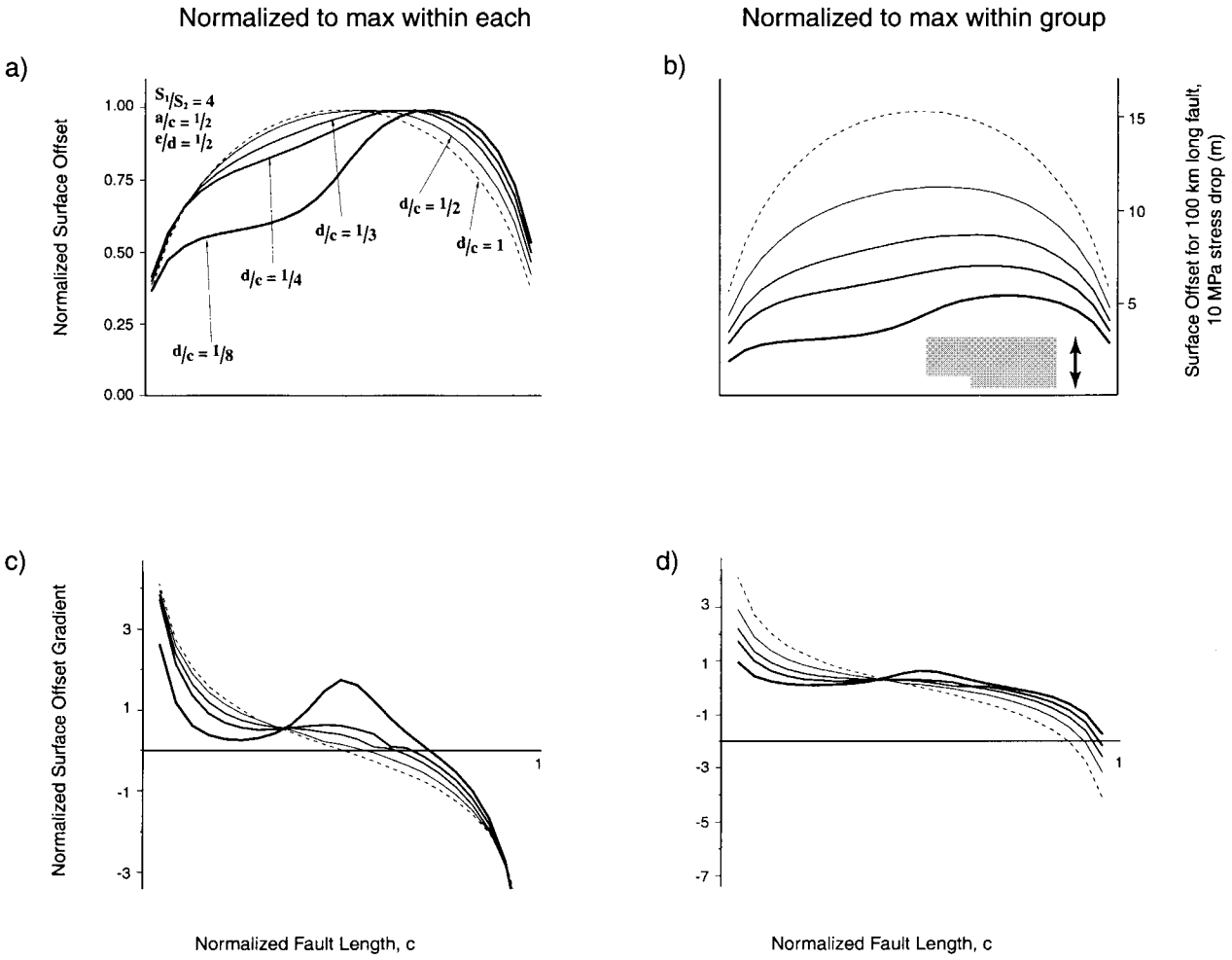

Figure 5. The effect of changing fault length relative to depth (*d*/*c*). Slip gradients at the segment boundary increased as *d*/*c* decreased, but the location of the peak slip remained relatively unchanged in each model. Letters refer to the same normalizations as in Figure 3.

caused the surface offsets in the Cholame segment to increase.

The central and southern Cholame and Carrizo segments last ruptured in the 1857 Fort Tejón earthquake (Sieh, 1978). In the central section of the Carrizo segment (~75 km), the data record low-magnitude offsets from 1857 that occur on multiple strands of the SAF. Trenching data (Sieh and Jahns, 1984) and repeated surveys (Grant and Donnellan, 1994) indicate greater offset in 1857 than each individual offset. In the northernmost Cholame segment (from 0 to 40 km), there are two offset events of approximately equal magnitude (~3.5 and ~7 m offsets between 10 and 23 km from Highway 46). The magnitude of each event is equal to the inferred offset magnitude of the 1857 earthquake in this area. Therefore, we interpreted these data as repeated characteristic ruptures within the Cholame segment. Offset of stratigraphic units across the SAF along the Cholame segment suggests approximately 3 m of slip in this area during the 1857 earthquake (Young *et al.,* 2000).

The 10- and 20-km interval data highlight two important trends: (1) overall displacement increases along strike of the fault between the 0–60-km section and the 60–100-km section of the fault (approximately at the segment boundary between the Cholame and Carrizo segments) and (2) the offset distribution in the northern Cholame segment (between 0 and 20 km) has several peaks that are well defined by the data (5 km interval data between 0 and 15 km; Fig. 9). Between 0 and 10 km, we infer offsets larger than 1 m to result from the 1857 Fort Tejón earthquake, which ruptured both the Cholame and Carrizo segments of the SAF.

Estimating Fault Segment Geometry for the Carrizo and Cholame Segments

We used microseismicity to define the fault geometry along the 1857 rupture surface (Fig. 10). The data include events $M_S > 1.5$ recorded between 1980 and 1989 (Hill, 1990). The microseismicity is projected onto a vertical plane approximately parallel to the SAF with a 30° discordance

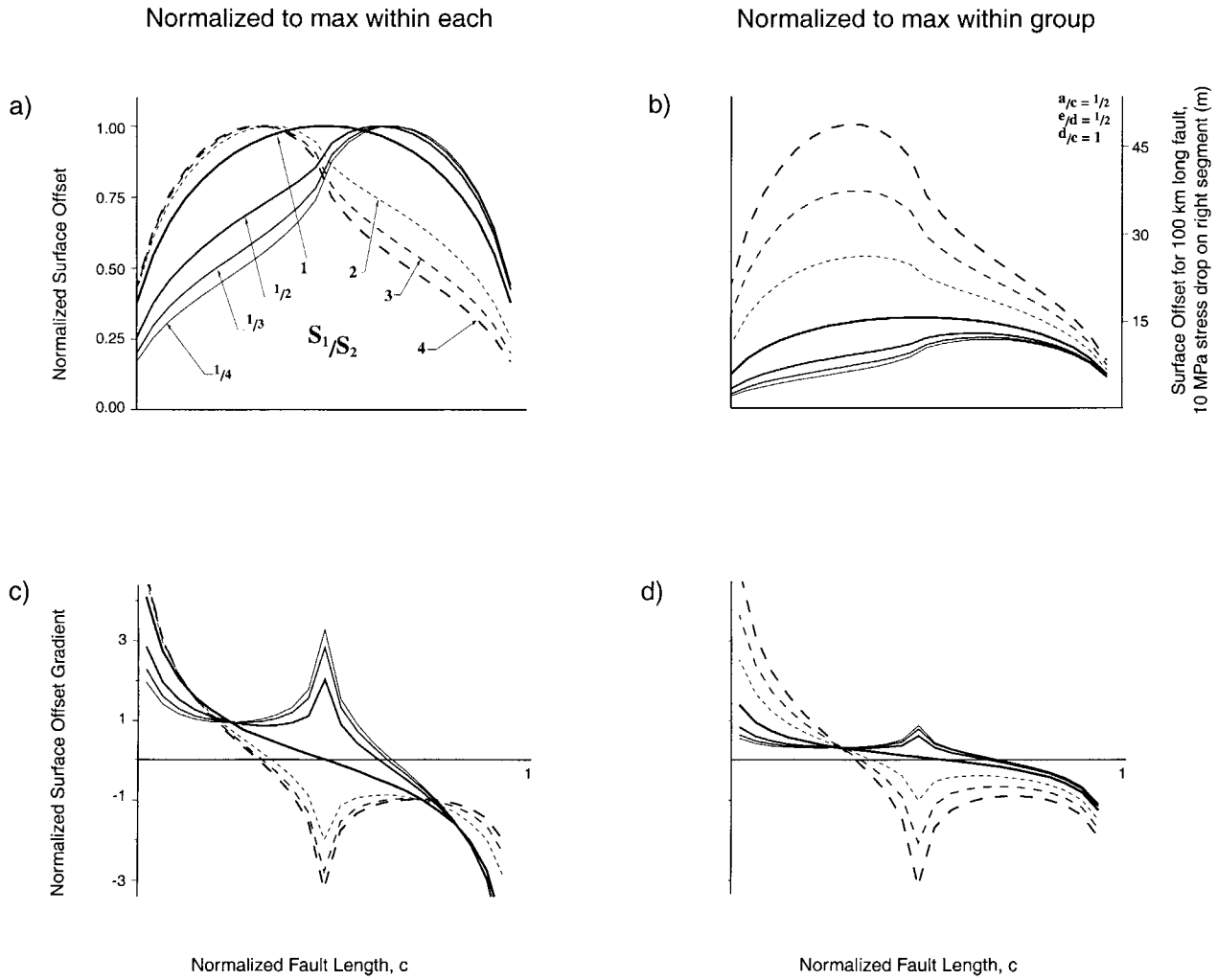

Figure 6. The effect of changing segment strength on the surface offsets. Slip is greater along the segment with greater strength. Greater strength contrasts lead to higher offset gradients at the segment boundary. The location of the peak offset is controlled by the location of the stronger segment but not by the magnitude of the strength contrast. Letters refer to the same normalizations as in Figure 3.

with the fault strike between 60 km along strike and the Big Bend of the SAF (bold line; top of Fig. 10). The misorientation in strike of the projection and fault planes results in a horizontal mislocation of seismic events in this zone, but the depth of the seismicity is unaffected. Microseismicity deepens from north to south approximately in the area of the Carrizo–Cholame boundary (Fig. 10). North of the boundary, the seismicity extends to a depth of 14–16 km. In addition, trilateration lines indicate that the Cholame segment is locked to a depth of 15 km (Harris and Archuleta, 1988). The exception to this depth range is a ~22-km-deep event, which we ignored when determining the geometry of the fault. South of the boundary, seismic activity extends to a depth of 22–25 km. Most of the events in this area are contained within the upper 22 km. We interpreted the seismogenic Cholame segment to extend to a depth of 14 km, while the seismogenic section of the Carrizo segment extends to a depth of 22 km. The lengths of the Cholame and Carrizo segments were modeled as 58 and 120 km long, respectively, so the ratios for this geometry are $a/c = 0.337$, $d/e = 0.364$, and $d/c = 0.145$. We used a 120-km-long rather than a 145-km-long Carrizo segment (WGCEP, 1988) because of numerical limitations in the model. The slightly shorter Carrizo segment modeled should well approximate the segment length defined by WGCEP (1988).

Determining Relative Fault Strengths from Offset Data

The filtered slip distributions were compared to model results of low-friction faults to determine strength contrasts between the Cholame and Carrizo segments necessary to produce the 1857 slip distribution (Fig. 9). We assumed that 9 m of slip accrued during the 1857 earthquake along the northern portion of the Carrizo segment (Sieh, 1978; Sieh

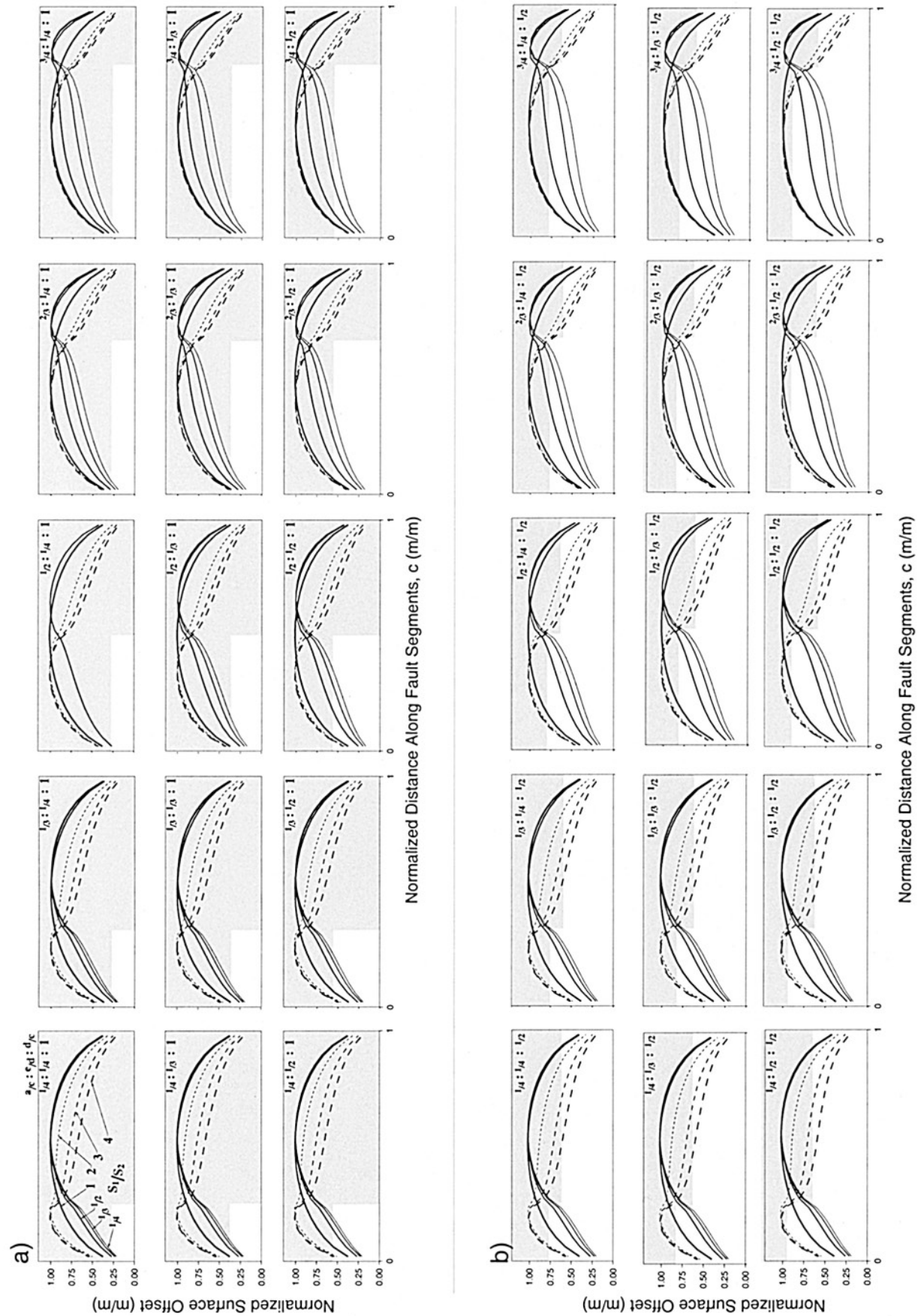

Figure 7. *See caption on p. XXX.*

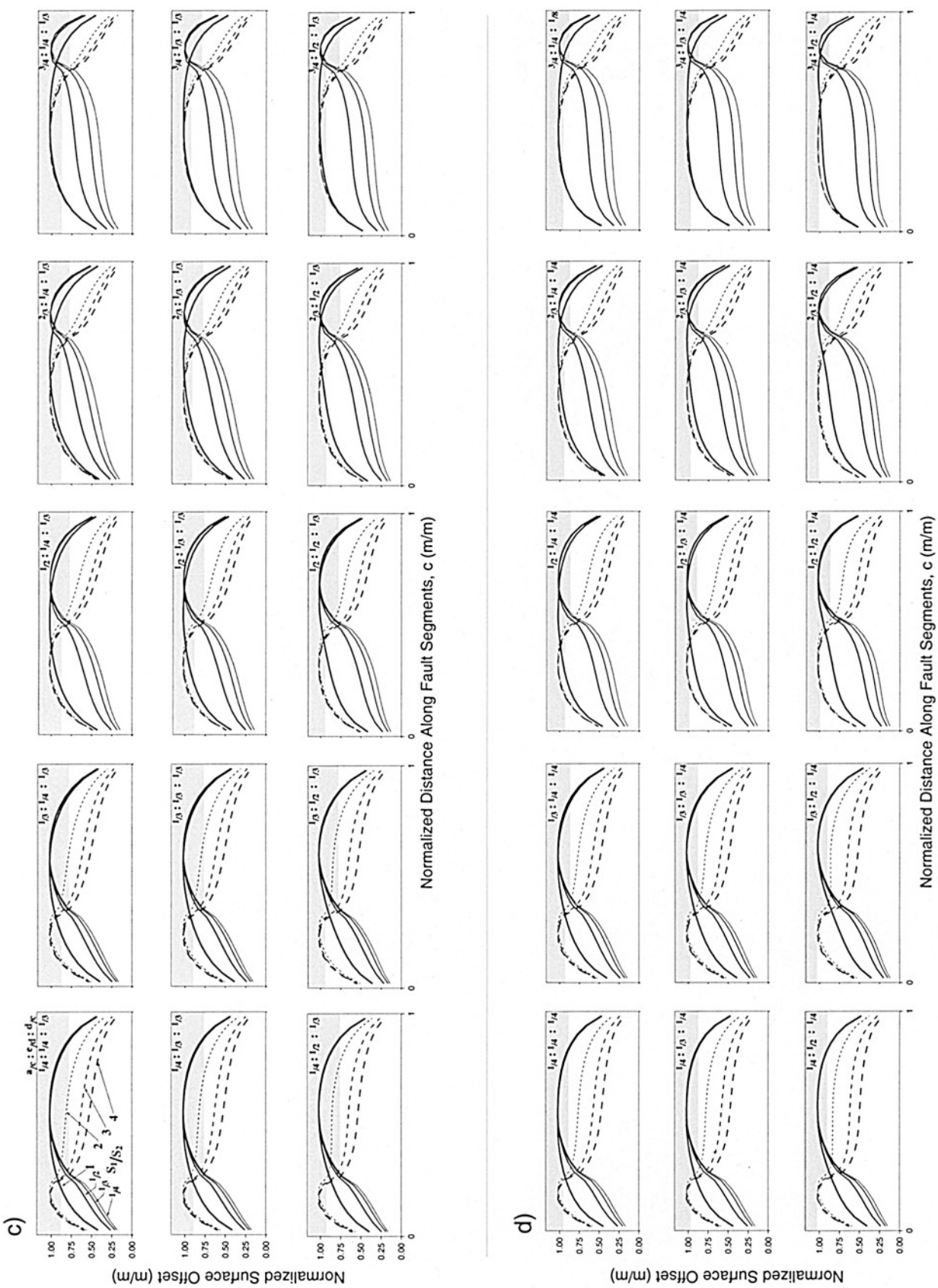

Figure 7. *(Continued).*

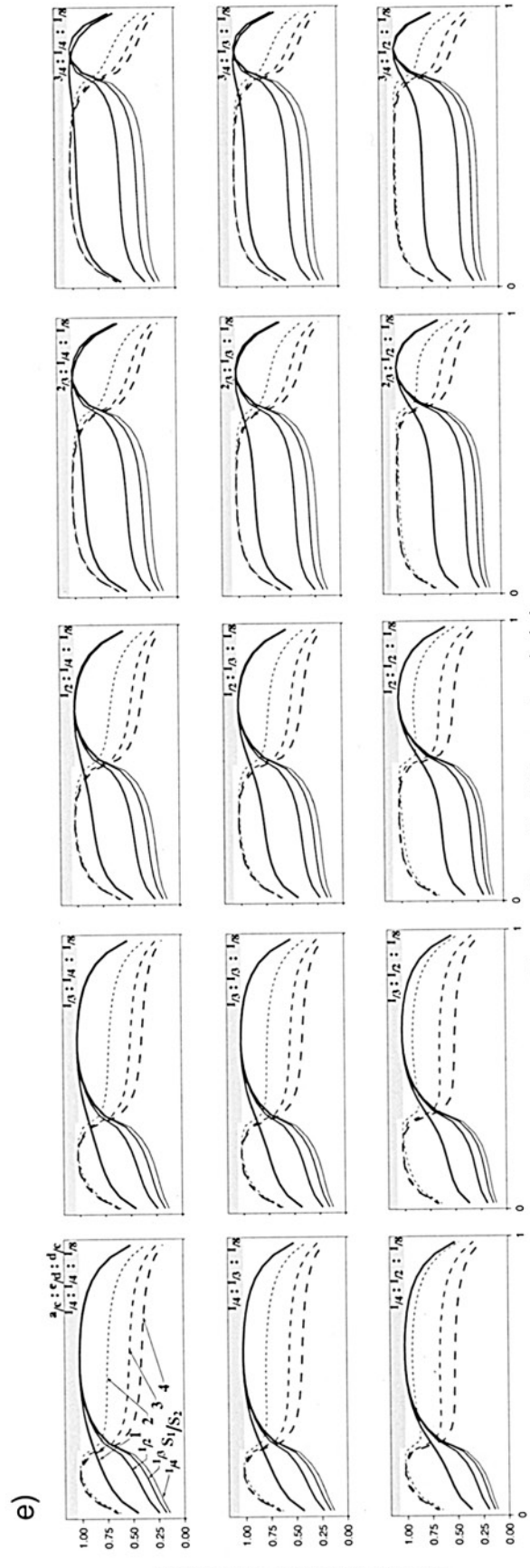

Figure 7. *(Continued).* Normalized surface offsets for all models. Each panel (a–e) shows a different variation of the depth-to-length ratio (*d*/*c*: 1, 1/2, 1/3, 1/4, 1/8). The gray shading in the background of the figures shows the relative geometry of the two fault segments. The columns isolate variations in the segment length ratio (*a*/*c*: 1/4, 1/3, 1/2, 2/3, 3/4). The rows in each panel isolate changes in the segment depth ratio (*e*/*d*: 1/4, 1/3, 1/2). For each chart, the curves correspond to strength contrasts ranging from 1/4 to 4. Labels on the top right corner of each figure show the geometry ratios as *a*/*c*:*e*/*d*:*d*/*c*.

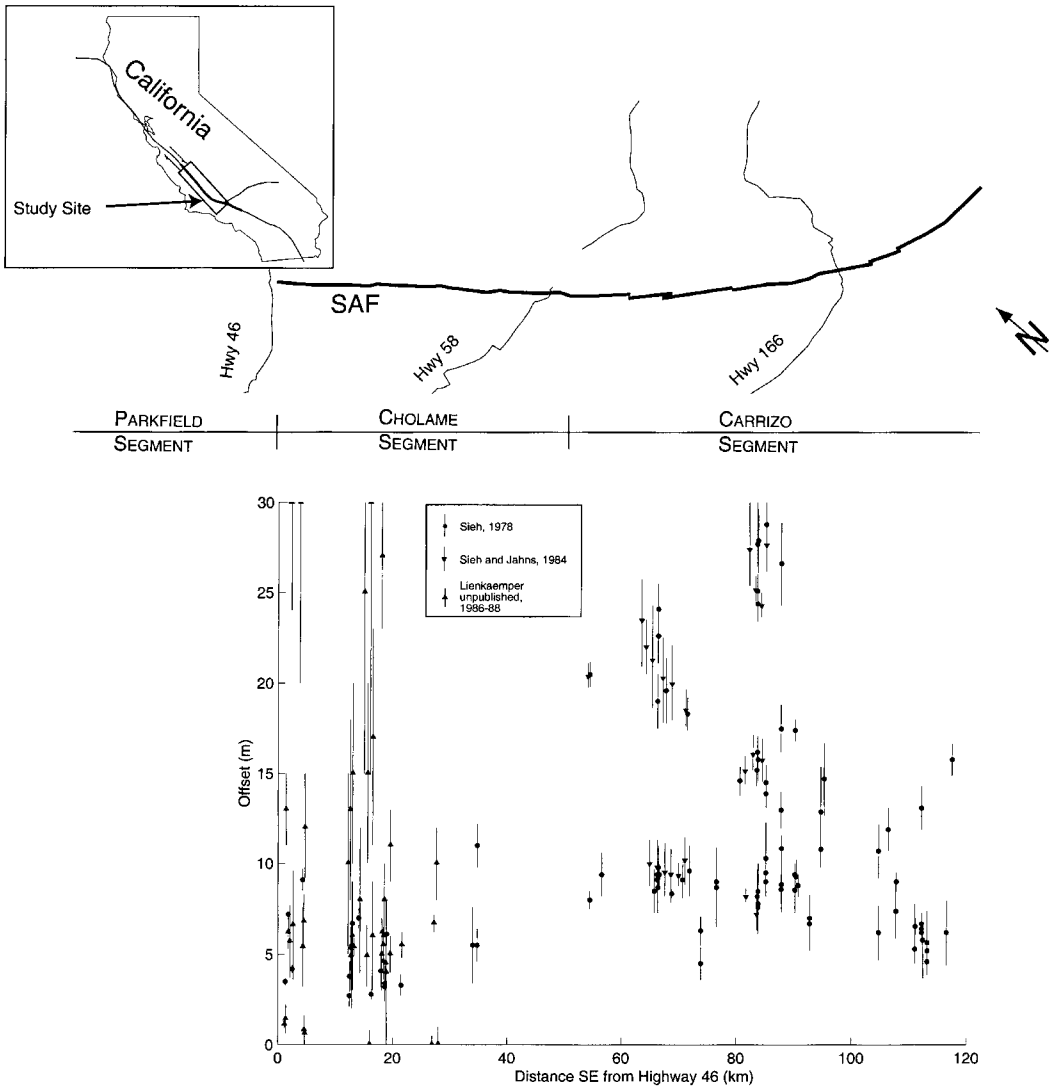

Figure 8. Offsets compiled from geomorphic observations along the Cholame and Carrizo segments of the SAF. The inset map shows the study location in California. Offset data are from Sieh (1978), Sieh and Jahns (1984), and Lienkaemper (submitted). Slip and the downdip extent of the locked SAF is larger in the Carrizo Segment than the Cholame segment (see Figure 10 for deepening of Carrizo Segment).

and Jahns, 1984), that the historic earthquake rupture record is complete, and that no further ruptures penetrated more than a few kilometers into the northern Cholame segment since 1857. The solid lines in Figure 9 show the expected surface offset distribution for the inferred down-dip geometry of the Cholame and Carrizo segments for strength ratios ($S_{\text{Cholame}}/S_{\text{Carrizo}}$) of 1, 2/3, 1/2, 1/3, and 1/4 for our estimated segment geometry.

The different estimations of the slip distributions during the 1857 Fort Tejón earthquake required different strength contrasts to produce the observed slip. Based on the simplifications of our model and the offset data, strength contrasts between 2/3 and 1/4 are required to produce the inferred 1857 Fort Tejón surface offset. In light of a possible ~3 m offset along the Cholame segment in 1857 (Young *et al.,* 2000), the inferred strength contrast may be closer to $1/2 > S_{\text{Cholame}}/S_{\text{Carrizo}} > 1/4$.

Discussion

In our models, along-strike variations in fault geometry are small, each fault segment undergoes a uniform stress drop during rupture, and rupture dynamics do not significantly impact the surface offset distribution. Deviations in strike may affect the long-term loading distribution acting along the fault. These complications are important; however, this study focused on coplanar fault segments.

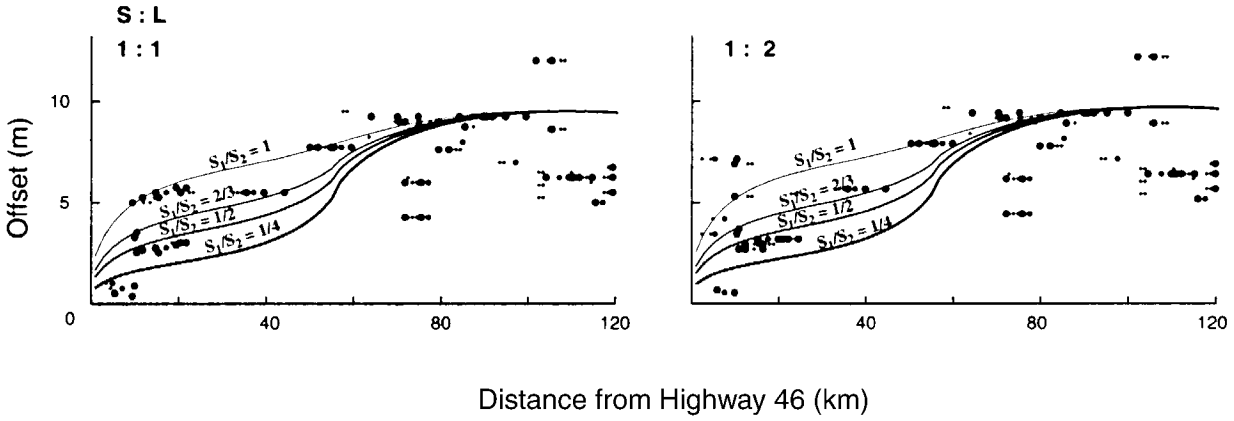

Figure 9. Modeled offsets overlain on reconstructed 1857 Fort Tejón earthquake offset distribution. Different sized points in this figure represent different sampling intervals: the small, medium, and large points represent 5, 10, and 20 km sampling intervals, respectively (see text for full description). We weighted each observer's data set according to the Sieh : Lienkaemper (S : L) values above the figures. Slip increases from the Cholame segment (left hand side of the graphs) into the Carrizo segment (right hand side of the graphs). Weighting Lienkaemper's data more strongly relative to Sieh's reduces the offset gradient at the segment boundary. The stress drops along the stronger segment required to produce the 9 m offset in the Carrizo are 8.71, 8.77, 8.80, and 8.92 MPa for $S_1/S_2 = 1$, 2/3, 1/2, and 1/4, respectively, assuming $G = 40$ GPa and $\nu = 0.25$. Under these conditions, the average total stress drop for each scenario would be 8.71, 8.06, 7.74, and 7.32 MPa, respectively. The largest difference between the stress drop along the strongest segment and the average stress drop along both segments is $<18\%$. The increase in the surface offset from the Cholame to the Carrizo segment (40–65 km) indicates a strength contrast of 2/3–1/4 between the Cholame and Carrizo segments.

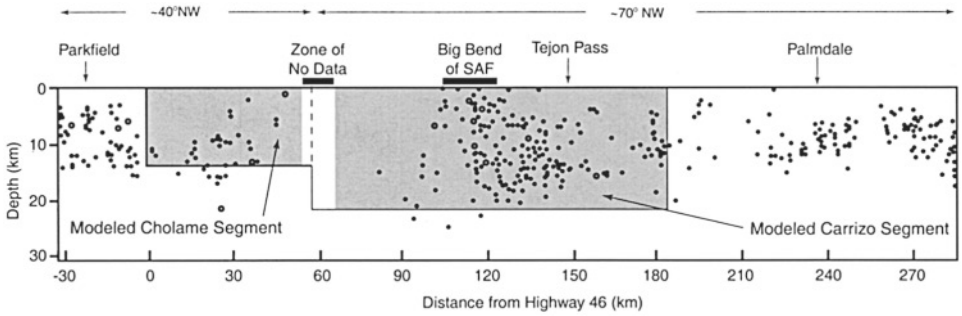

Figure 10. Microseismicity along the San Andreas Fault between Parkfield, California and southeast of Palmdale, California. Microseismicity is taken from Hill *et al.* (1990). The gray rectangles show our inferred fault geometry from the microseismicity. Strikes noted at the top of the figure show the strike of the vertical plane onto which the microseismicity is projected. In the region between 58 and 120 km, the projection plane is misoriented relative to the fault plane.

The fault surface may not experience a uniform stress drop during rupture because of a complex loading history on the fault plane. This loading history may result in along-strike variations in stress release that may mimic strength contrasts during an event. The minimum strength contrasts required to fit the 1857 offsets require the Carrizo segment to have large pre-existing shear stresses relative to the Cholame segment. For instance, we consider the limiting case of two adjacent fault segments with the same strength. Prior to loading and rupture, one segment has residual stresses just below the segment's critical strength, while the other has no residual stress acting along its surface. If both segments are instantaneously loaded and rupture, the stress drop along the segment with residual stress will be no greater than twice its critical strength. In contrast, the segment with no residual stress will experience a stress release equal to its critical strength. Therefore, residual stresses along different segments of similar strength are unlikely to produce an apparent

strength contrast larger than 1:2. Our inferences along the Cholame and Carrizo segments suggest this value is towards the lower bound of the strength contrasts. We cannot dismiss the possibility that the 1857 offset distribution was produced by these pre-existing stresses, but most data may require unreasonably large prestress differences between the two segments. In addition, offsets in the Carrizo suggest repeated large offsets over several earthquakes. These repeated offsets require large prestresses to exist before each rupture along the Carrizo segment. Therefore, these repetitious large offsets may suggest a persistent strength contrast between the Cholame and Carrizo segments rather than pre-existing stresses.

Our models also indicate that a multisegment fault that is slipping at a constant rate along its length may undergo separate catch-up events to resolve differences in slip created by variations in segment geometry or strength. In the case of the Cholame and Carrizo segments of the SAF, the potentially weaker Cholame segment may necessitate these types of catch-up events in order to maintain the constant 35 mm/yr of slip along the SAF in this area. While our analyses of geomorphic offsets do not resolve such events, other modeling studies (e.g., Ward, 1997) produce similar behavior.

In general, our inferred strength contrast is dependent on both the simplification of reality of our model and the interpretation of an 1857 offset distribution based on noisy data. While the $2/3 < S_{\text{Cholame}}/S_{\text{Carrizo}} < 1/4$ strength contrast is consistent with a majority of the offset data, the data are nonetheless ambiguous. However, it is clear that there was probably a significant reduction in slip along the Cholame segment relative to the Carrizo segment during the 1857 event. This reduction is consistent with at least a small reduction in segment strength along the Cholame relative to the Carrizo segment. Therefore, while we cannot preclude similar strengths of the two segments based on the scattered data and our simplification of fault rupture, our results suggest that a strength contrast of some sort may exist between the two segments.

Fault segmentation may be produced by a number of different mechanisms including fault segment geometry and strength contrasts. The interaction of fault geometry and strength contrasts may lead to complex rupture sequences caused by either constant loading or constant slip-rate conditions on the fault (e.g., Ward, 1997). Event sequences observed in the stratigraphic and/or geomorphic record may record a brief window of a more complex rupture history that is best understood in terms of these interacting effects. The results of this study highlight the controls on fault segmentation and provide a method to determine fault segment properties that may be used in more sophisticated models (such as those of Ward, 1997).

Conclusions

Fault segmentation may arise from changes in the fault geometry and strength and may control the extent and magnitude of ruptures. We used elastic dislocation models to understand these effects on surface offsets along a pair of vertical, coplanar, adjacent, strike-slip fault segments. These models indicated that: (1) the position of the maximum surface offset gradient corresponds to the segment boundary; (2) the relative steepness of the surface offset gradient is related to the ratio of the depth of the deep segment relative to the shallow segment, and (3) the difference in peak displacement between each segment is strongly influenced by the ratio of the total fault depth to the total fault length. We used this mechanical model in conjunction with surface offsets to estimate a strength contrast of 2/3–1/4 between the Cholame and Carrizo segments of the SAF.

Acknowledgments

The authors wish to acknowledge James Lienkaemper for sharing the data he collected along the Cholame segment of the SAF, Mark Zoback for his early commentary and support of this effort, the Southern California Earthquake Center, Steve Ward for several thorough reviews of the manuscript, and the NASA Earth Systems Science Fellowship. SCEC is funded by NSF Cooperative Agreement EAR-8920136 and USGS Cooperative Agreements 14-08-0001-A0899 and 1434-HQ-97AG01718. The SCEC contribution number for this article is 470.

References

Andrews, D. J. (1976). Rupture propagation with finite stress in antiplane strain, *J. Geophys. Res.* **81,** 3575–3582.

Andrews, D. J. (1994). Dynamic growth of mixed-mode shear cracks, *Bull. Seism. Soc. Am.* **84,** 1184–1198.

Arrowsmith, R., K. McNally, and J. Davis (1997). Potential for earthquake rupture and M 7 earthquakes along the Parkfield, Cholame, and Carrizo segments of the San Andreas Fault, *Seism. Res. Lett.* **68,** 902–916.

Ben-Zion, Y., and J. R. Rice (1995). Slip along a crustal-scale fault governed by rate- and state-dependent friction and inertial elastodynamics, *EOS* **76,** 405.

Bürgmann, R., P. Segall, M. Lisowski, and J. Svarc (1997). Postseismic strain following the 1989 Loma Prieta earthquake from GPS and leveling measurements, *J. Geophys. Res. B* **102,** 4933–4955.

Day, S. M. (1982). Three-dimensional simulation of spontaneous rupture; the effect of nonuniform prestress: special papers on the dynamic characteristics of faulting inferred from recordings of strong ground motion, *Bull. Seism. Soc. Am.* **72,** 1881–1902.

Erikson, L. L. (1987). DIS3D: a three dimensional dislocation program with applications to faulting in the earth, *M.S. Thesis,* Stanford University, Stanford, California.

Grant, L. B., and A. Donnellan (1994). 1855 and 1991 surveys of the San Andreas Fault: implications for fault mechanics, *Bull. Seism. Soc. Am.* **84,** 241–246.

Harris, R. A., and R. J. Archuleta (1988). Slip budget and potential for a *M*7 earthquake in central California, *Geophys. Res. Lett.* **15,** 1215–1218.

Hickman, S. (1991). Stress in the lithosphere and the strength of active faults, *Rev. Geophys.* **29,** 759–775.

Hill, D. P., J. P. Eaton, and L. M. Jones (1990). Seismicity, 1980–1986, in *The San Andreas Fault System, California,* R. E. Wallace (Editor), *U.S. Geol. Surv. Prof. Pap. 1515,* 115–151.

Jaeger, J. C., and N. G. W. Cook (1969). *Fundamentals of Rock Mechanics,* Methuen, London, 513 pp.

Lienkaemper, J. J., and T. A. Sturm (1989). Reconstruction of a channel

offset in 1857(?) by the San Andreas Fault near Cholame, California, *Bull. Seism. Soc. Am.* **79,** 901–909.

Muskhelishvili, N. I. (1954) *Some Basic Problems of the Mathematical Theory of Elasticity,* P. Noordhoff Ltd., Groningen, The Netherlands.

Pollitz, F. F. (1992). Postseismic relaxation theory on the spherical Earth, *Bull. Seism. Soc. Am.* **82,** 422–453.

Rubin, A. M. (1988). Dike propagation and crustal deformation in volcanic rift zones, *Ph. D. Thesis,* Stanford University, Stanford, California.

Schwartz, D. P., and K. J. Coppersmith (1984). Fault behavior and characteristic earthquakes: examples from the Wasatch and San Andreas fault zones, *J. Geophys. Res.* **89,** 5681–5698.

Segall, P., and D. D. Pollard (1980). The mechanics of discontinuous faults, *J. Geophys. Res.* **85,** 4337–4350.

Sieh, K. E. (1978). Slip along the San Andreas fault associated with the great 1857 earthquake, *Bull. Seism. Soc. Am.* **68,** 1421–1448.

Sieh, K. (1996). The repetition of large-earthquake ruptures, *Proc. Natl. Acad. Sci.* **93,** no. 9, 3764–3771.

Sieh, K. E., and R. H. Jahns (1984). Holocene activity of the San Andreas Fault at Wallace Creek, California, *Geol. Soc. Am. Bull.* **95,** 883–896.

Sokolnikoff, I. S. (1956). *Mathematical Theory of Elasticity,* Second edition, McGraw-Hill, New York, 475 pp.

Thomas, A. P., and T. K. Rockwell (1996). A 300- to 550-year history of slip on the Imperial fault near the U.S.–Mexico border: missing slip at the Imperial fault bottleneck, *J. Geophys. Res. B* **101,** 5987–5997.

Wald, D. J., and T. H. Heaton (1992). Spatial and temporal distribution of slip for the 1992 Landers, California, earthquake, *Bull. Seism. Soc. Am.* **84,** 668–691.

Ward, S. N. (1997). Dogtails versus rainbows: synthetic earthquake rupture models as an aid in interpreting geological data, *Bull. Seism. Soc. Am.* **87,** 1422–1441.

Working Group on California Earthquake Probabilities (WGCEP) (1988). Probabilities of large earthquakes occurring in California on the San Andreas fault, *U.S. Geol. Surv. Open-File Rept. OF 88-398,* 62 pp.

Working Group on Northern California Earthquake Potential (WGNCEP) (1996). Database of potential sources for earthquakes larger than magnitude 6 in Northern California, *U.S. Geol. Surv. Open-File Rept. 96-0705,* 53 pp.

Young, J. J., L. Colini, J. R. Arrowsmith, and L. Grant (2000). Recent surface ruptures along the Cholame segment of the San Andreas Fault, *EOS* **81,** 925.

Zoback, M. D., M. L. Zoback, V. S. Mount, J. Suppe, J. P. Eaton, D. Oppenheimer, P. Reasenberg, L. Jones, C. B. Raleigh, I. G. Wong, O. Scotti, and C. Wentworth (1987). New evidence on the state of stress of the San Andreas fault system, *Science* **238,** 1105–1111.

Active Tectonics Research Group
Department of Geology
Arizona State University
(G.H., J R.A., E.S.)

Manuscript received 22 September 2000.